APPLIED SCIENCES AND ENGINEERING

Reprogramming cellular senescence in the tumor microenvironment augments cancer immunotherapy through multifunctional nanocrystals

Zheng Wang[1]†, Yinglu Chen[2,3]†, Hui Fang[3], Kai Xiao[3], Ziping Wu[3], Xiaochun Xie[3], Jie Liu[4], Fangman Chen[3], Yi He[5], Liang Wang[4], Chao Yang[4]*, Renjun Pei[1]*, Dan Shao[2,3]*

Harnessing the immunogenic potential of senescent tumor cells provides an opportunity to remodel tumor microenvironment (TME) and boost antitumor immunity. However, this potential needs to be sophisticatedly wielded to avoid additional immunosuppressive capacity of senescent cells. Our study shows that blocking the JAK2/STAT3 pathway enhances immunogenic efficacy of Aurora kinase inhibitor alisertib (Ali)–induced senescence by reducing immunosuppressive senescence-associated secretory phenotype (SASP) while preserving immunogenic SASP. Hypothesizing that SASP reprogramming with Ali and JAK2 inhibitor ruxolitinib (Rux) will benefit cancer immunotherapy, we create nanoparticulate crystals (Ali-Rux) composed of Ali and Rux with a fully active pharmaceutical ingredient. Immunization with Ali-Rux–orchestrated senescent cells promotes stronger activation of antigen-presenting cells, enhancing antitumor immune surveillance. This approach remodels the TME by increasing $CD8^+$ T cell and NK recruitment and activation while decreasing MDSCs. Combined with PD-L1 blockade, Ali-Rux elicits a durable antitumor immune response, suggesting the TME reshaping approach as a potential cancer immunotherapy.

INTRODUCTION

After suffering countless successes and setbacks over the past decade, immunotherapy is now at the forefront of cancer research, especially for many previously untreatable malignancies (*1*–*3*). Cancer immunotherapy has been harnessed as an important means to indirectly kill tumor cells through leveraging the principle of reactivating the immune system (*4*, *5*). The tumor microenvironment (TME) and the patterns of local interactions between malignant cells, stromal cells, and immune cells have been extensively considered to be essential for the survival of cancer cells against treatments (*6*, *7*). Both cellular and molecular components of the TME can serve to orchestrate the efficacy of immunotherapy and are critical to explore the next generation of cancer therapeutics (*8*, *9*). In such a scenario, the immunosuppressive TME can be profoundly modulated to an immunogenic TME via the combination of immune checkpoint blockade (ICB), immunogenic adjuvants, and immunogenic cell death (ICD)–based strategies (*10*–*14*). Among them, the vaccine-like effect of ICD can be attributed to the release of tumor-associated antigens, damage-associated molecular patterns (DAMPs), and proinflammatory cytokines, leading to the recruitment and activation of antigen-presenting cells (APC) as well as stimulation of $CD8^+$ cytotoxic T cells (CTLs) (*15*–*19*). Nevertheless, it is still a challenge to elicit a sustained antitumor immune response to reeducate the TME, which might provide fruitful directions for developing immunotherapeutic paradigms against cancer.

Senescence is a cellular response to various stress and damage signals, which is characterized as a physiological process to eliminate aberrant, damaged, or unwanted cells (*20*–*22*). Such a response consists of irreversible proliferative arrest together with the production of multiple senescence-associated secretory phenotypes (SASPs), which results in the activation of immune system for the clearance of senescent cells, thereby maintaining tissue homeostasis (*23*–*25*). Different from normal cells, cancer cells are usually exposed to a multitude of stressors, contributing to the regulation of the TME in a complex manner of senescence (*26*, *27*). A unique biological outcome of cancer therapy is the induction of cellular senescence, which is associated with a positive or negative impact on therapeutic outcomes (*24*, *28*). The dynamic nature of the SASPs and its different way of regulating immune responses and the surrounding TME contribute to the many contrasting physiological phenomena associated with senescence (*29*, *30*). On the one hand, the presentation of senescence-associated self-antigens together with the release of immunogenic SASPs recruits and activates immune cells for tumor regression, promoting antitumor immunity that enhances therapeutic effect (*31*, *32*). On the other hand, uncontrollable accumulation of immunosuppressive SASPs following a range of cancer therapies can stimulate tumor resistance and metastasis, leading to therapy failure and tumor relapse (*33*, *34*). Thus, tailored modulation of the SASPs, which is necessary to contribute to maintaining SASP-mediated anticancer pathway while inhibiting or abolishing the bad effects of SASPs, is key to representing an emerging immunotherapeutic paradigm in the fight against cancer. With these findings in mind, we hypothesize that the combination of a senescence inducer and SASP regulator may generate maximal antitumoral SASPs with minimal protumoral SASPs in the TME, offering an opportunity to leverage immunogenic potential of

[1]Suzhou Institute of Nano-Tech and NanoBionics, Chinese Academy of Sciences, Suzhou 215123, China. [2]State Key Laboratory of Oral Diseases and National Clinical Research Center for Oral Diseases and Department of Oral and Maxillofacial Surgery, West China Hospital of Stomatology, Sichuan University, Chengdu, Sichuan 610041, China. [3]National Engineering Research Center for Tissue Restoration and Reconstruction, South China University of Technology, Guangzhou, Guangdong 510006, China. [4]Department of Orthopedics, Academy of Orthopedics-Guangdong Province, Orthopedic Hospital of Guangdong Province, Guangdong Provincial Key Laboratory of Bone and Joint Degenerative Diseases, The Third Affiliated Hospital of Southern Medical University, Guangzhou 510630, China. [5]Department of Rheumatology and Immunology, The Third Affiliated Hospital, Southern Medical University, Guangzhou 510630, China.
*Corresponding author. Email: charisyang910@gmail.com (C.Y.); rjpei2011@sinano.ac.cn (R.P.); stanauagate@outlook.com (D.S.)
†These authors contributed equally to this work.

senescence to elicit antitumor immunity and potentially complement anticancer therapies.

To meet the challenges of senescence-based cancer immunotherapy, we herein propose a combined strategy that integrates senescence inducers and SASP regulators to enhance immune responses and prevent tumor relapse. We first revealed the SASP profile of breast cancer cells after treatment with alisertib (Ali), an inhibitor of Aurora kinases, which is known to induce cellular senescence by blocking mitosis. Having deciphered the phenotypic SASP after receiving three different SASP regulators, the Janus kinase 2 (JAK2)/signal transducers and activators of transcription 3 (STAT3) inhibitor ruxolitinib (Rux) was selected to best reduce the protumoral SASP without interfering with the antitumoral SASP or abolishing growth arrest. We then created nanoparticulate crystals composed of Ali and Rux with a fully active pharmaceutical ingredient content for oral administration. After accumulating in the TME, Ali-Rux efficiently induces tumor senescence and reprograms SASP release. Compared with ICD or nonsenescent cells, immunization with Ali-Rux–orchestrated senescent cells promoted better activation and maturation of APCs, leading to potentiated antitumor immune surveillance. Consequently, such a nanodrug promoted tumor immunogenicity while reversing immunosuppression in the TME by increasing the recruitment and activation of $CD8^+$ T cells and natural killer (NK) cells while decreasing the tumor infiltration of myeloid-derived suppressor cells (MDSCs). When combined with anti-PD-L1 (αPD-L1) antibody, nanodrugs elicited an excellent eradication of primary and metastatic tumors along with fewer side effects. Our study offers a promising senescence modulation strategy to rewire the TME, thus facilitating senescence-based cancer immunotherapy.

RESULTS

Ali successfully induced the senescence of 4T1 cells after 3 days of coincubation, as evidenced by the change in morphology (fig. S1) and increase in senescence-associated β-galactosidase (SAβG) activity (Fig. 1, A and B). To investigate the production of SASPs, we identified the repertoire of the secretory profile in the medium of 4T1 cells after incubated with Ali by a cytokine antibody array, demonstrating that classic SASPs, including granulocyte-macrophage colony-stimulating factor (GM-CSF), macrophage colony-stimulating factor (M-CSF), interleukin-6 (IL-6), IL-10, IL-13, intercellular adhesion molecule–1 (ICAM-1), chemokine (C-CC motif) ligand 5 (CCL5), and Monocyte Chemoattractant Protein-1 (MCP-1), were elevated in response to Ali treatment (Fig. 1C and fig. S2). Aiming to find proper SASP regulators for decreasing immunosuppressive SASPs induced by Ali, three types of compounds targeting SASP regulators, including the nuclear factor κB (NF-κB) inhibitor BAY 11-7082 (BAY), the p38MAPK inhibitor SB203580 (SB2), and the JAK2/STAT3 inhibitor Rux, were incubated with Ali-treated 4T1 cells. The development of cellular senescence induced by Ali was not obviously influenced by the addition of Rux and SB2 (Fig. 1A and fig. S3). However, SAβG activity and growth arrest were slightly decreased in the Ali-treated cells when incubated with BAY (figs. S3 and S4), suggesting that BAY modestly weakened the induction of senescence by Ali. Rux reduced only a majority of immunosuppressive SASPs, including GM-CSF, M-CSF, IL-10, and IL-13, which were previously shown to recruit and activate MDSCs, but retained high levels of immunostimulatory SASPs involved in senescence surveillance, such as ICAM-1, CCL5, and MCP-1, in Ali-induced senescent 4T1 cells (Fig. 1C). In contrast, BAY and SB2 substantially decreased the generation of most SASPs (Fig. 1C). Only GM-CSF and M-CSF were slightly down-regulated by Rux in the untreated 4T1 cells, suggesting that Rux had limited effect in nonsenescent cancer cells (fig. S5). To explore the effect of the secretome on tumor growth in vivo, mice received untreated 4T1 cells with condensed SASPs from pretreated senescent 4T1 into their mammary fat pads (Fig. 1D). Most tumors were visible in the mice after 6 days of inoculation with untreated 4T1 cells (Fig. 1E and fig. S6). Notably, tumor progression was slightly expedited in mice inoculated with 4T1 cells with condensed SASPs from Ali-pretreated cells, suggesting that Ali-derived SASPs had a risk of promoting tumor progression. In contrast, tumor progression was remarkably delayed when mice were inoculated with 4T1 cells with Ali plus SASP regulators in comparison to that inoculated with free 4T1 cells, and the slowest tumor growth was detected in the Ali plus Rux groups (Fig. 1E and fig. S6). Similarly, immunofluorescence (IF) staining and flow cytometry analysis together showed that SASPs induced by Ali plus Rux triggered the strongest increase in the number of $CD8^+$ T and NK cells and the greatest reduction in the presence of MDSCs in the TME among all the treatment groups (Fig. 1, F and G, and fig. S7). Collectively, these results demonstrated that Rux alleviated the Ali-induced immune TME via increasing the immunostimulatory cell infiltration and decreasing the recruitment of immunosuppressive cells in tumors, supporting the proposed strategy of integrating the senescence inducer Ali with the SASP regulator Rux for further immunotherapy.

To improve the bioavailability and tumor targeting of Ali and Rux, we next fabricated a carrier-free nanodrug (Ali-Rux) that was only coassembled by Ali and Rux via a turbulent mixing method termed flash nanocomplexation (Fig. 2A). The binding energy (−4.3 kJ/mol) between Ali and Rux was determined by molecular dynamic simulations (fig. S8), indicating the possibility of the self-assembly of Ali and Rux. Beyond hydrophobic interactions, the hydrogen bond and van der Waals forces determined by the interaction region indicator assay contributed to driving the interaction between Ali and Rux (Fig. 2B). Such nanoparticulate crystals exhibited a uniform structure with a size of ≈50 nm, good dispersibility, and a negative surface charge (−8.98 mV) when the mass ratio of Ali to Rux is 2 to 3 (Fig. 2C and figs. S9 and 10). The ultraviolet-visible (UV-vis) spectrum showed that Ali-Rux had the same characteristic absorption peak at 311 nm as Ali and Rux (Fig. 2D), indicating the coexistence of Ali and Rux in Ali-Rux. The Fourier transform infrared (FTIR) spectra of Ali-Rux presented the typical peaks of —CN stretching vibration at 2250 cm^{-1} and —C═O— in aromatic aldehydes stretching vibration at 1650 to 1750 cm^{-1}, suggesting the preservation of both Ali and Rux (Fig. 2E). Furthermore, the FTIR results also revealed the formation of hydrogen bonding network with a classic absorption peak near 3300 cm^{-1} (—OH vibrational peak), which indicated the assembly of Ali and Rux. X-ray diffraction (XRD) analysis revealed amorphous nanocrystals of Ali-Rux (Fig. 2F). Through high-performance liquid chromatography (HPLC) analysis, the individual drug loading percentages of Ali and Rux were determined as 38.3 and 61.7%, respectively.

Given that the stability and dissolution rates of poorly water-soluble molecules can be improved by nanocrystallization, we found that Ali-Rux displayed sustained release of Ali and Rux in simulated body fluid (SBF). The cumulative release of Ali and Rux from Ali-Rux reached 73.2 and 78.1% over a 72-hour period (Fig. 2G), respectively, which were much slower than the release of free Ali or Rux

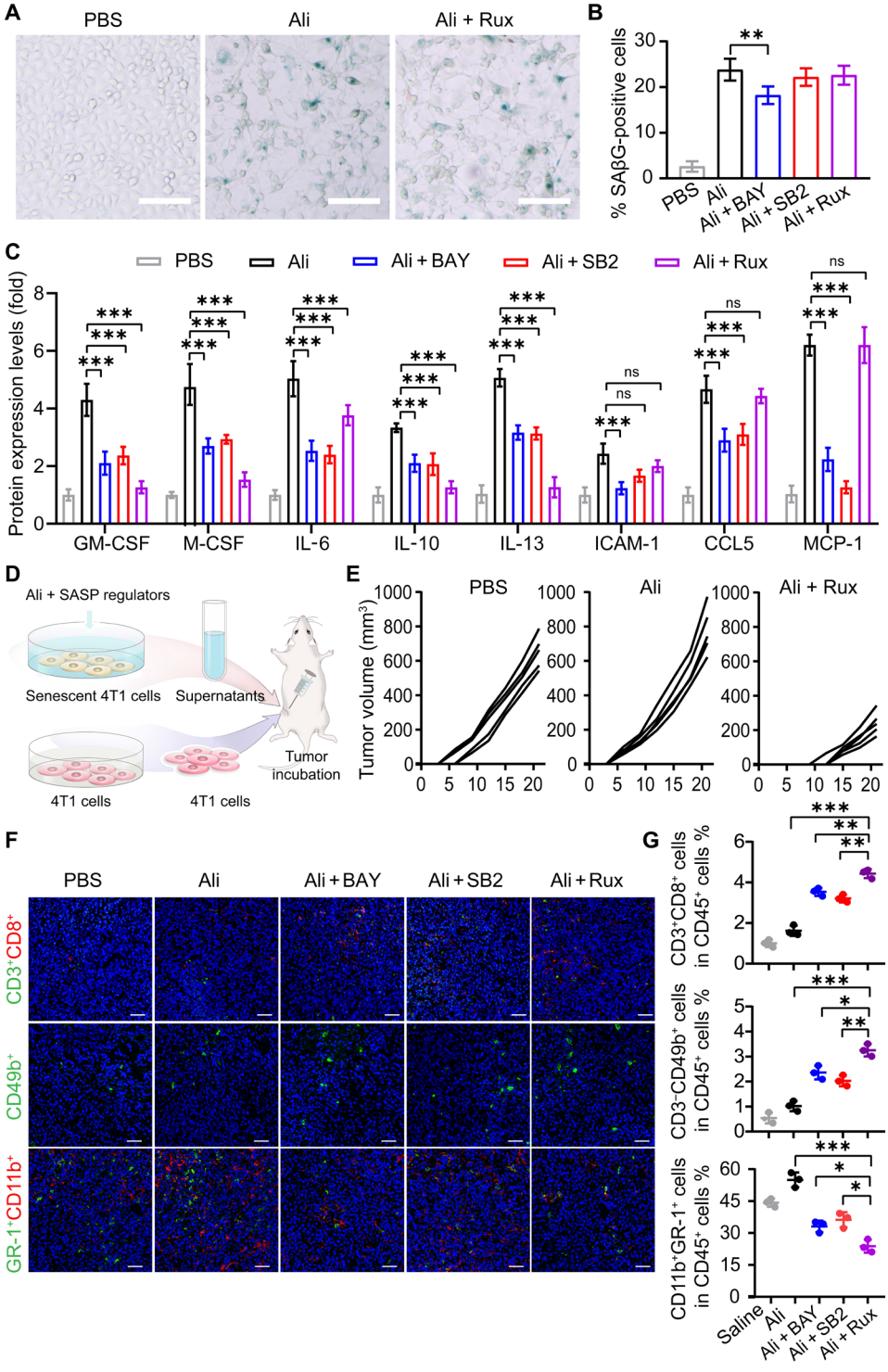

Fig. 1. Screening SASP regulators combined with Ali to induce selective cellular senescence for tumor inhibition. (**A**) SAβG staining of 4T1 cells after incubated with various formulations for 3 days. Scale bars, 100 μm. (**B**) Percentage of SAβG-positive 4T1 cells after incubated with various formulations for 3 days, $n = 5$, $^{**}P < 0.01$. (**C**) Quantitative enzyme-linked immunosorbent assays (ELISAs) for the cytokine protein profiles of culture medium from 4T1 cells after various treatments, $n = 3$. (**D**) Scheme of the protocol that inoculating untreated 4T1 cells and condensed supernatants into the mammary fat pads of mice. (**E**) Tumor growth curve of the mice after inoculation with condensed cell medium from pretreated 4T1 cells and untreated 4T1 cells. The pretreated 4T1 cells were incubated with PBS, Ali, Ali + BAY, Ali + SB2, and Ali + Rux for 3 days before inoculation. (**F**) IF analysis of $CD8^+$ T cells, NK cells, and MDSCs in tumor tissues. Scale bars, 50 μm. (**G**) Tumor infiltration of $CD8^+$ T cells, NK cells, and MDSCs by flow cytometry analysis. All data are mean ± SD, $n = 3$. $^*P < 0.05$, $^{**}P < 0.01$, and $^{***}P < 0.001$. ns, not significant.

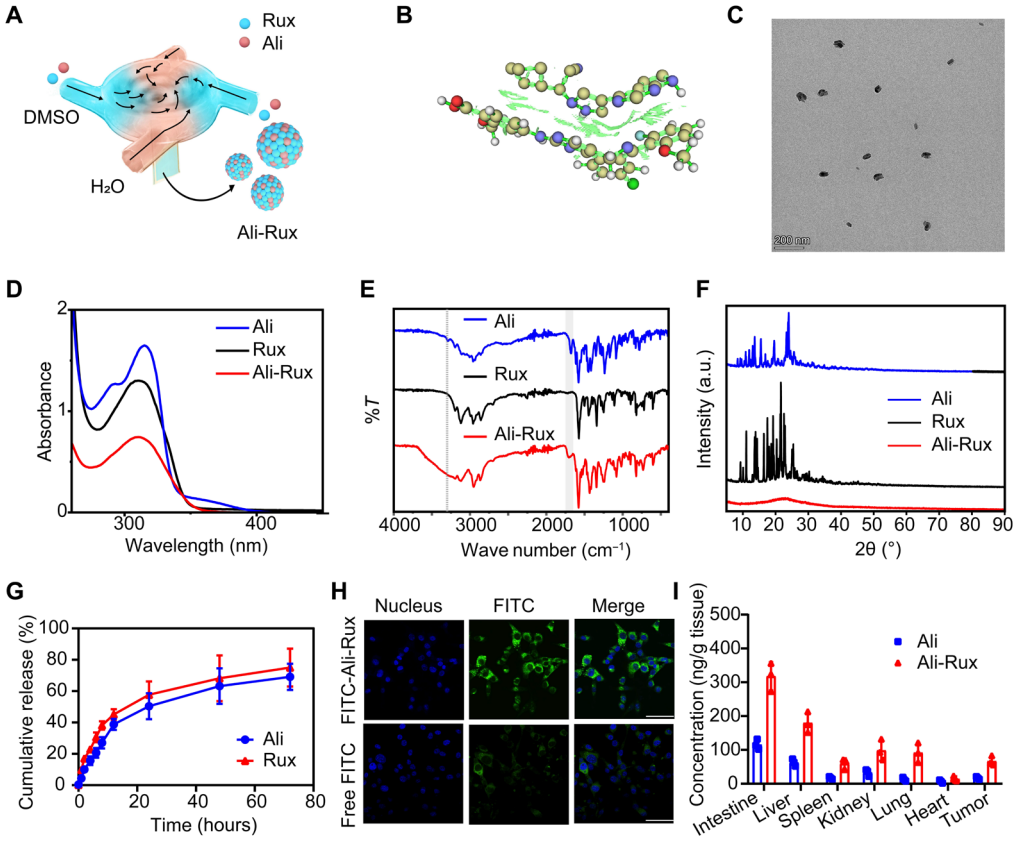

Fig. 2. Fabrication and characterization of Ali-Rux nanocrystals. (**A**) Scheme of the fabrication of Ali-Rux by a turbulent mixing method. (**B**) Three-dimensional isosurfaces of Ali and Rux. (**C**) Transmission electron microscopy image of Ali-Rux. Scale bar, 200 nm. (**D** to **F**) UV-vis absorption spectra (D), FTIR spectra (E), XRD spectra (F) and of Ali-Rux. (**G**) Drug release profile of Ali-Rux in SBF. (**H**) Fluorescent image of 4T1 cells after incubation with FITC-labeled Ali-Rux. (**I**) Ali concentrations in organs and tumor at 8 hours after the oral administration with free Ali and Ali-Rux. All data are mean ± SD, $n = 3$. DMSO, dimethyl sulfoxide; a.u., arbitrary units.

(fig. S11), indicating the sustained and coordinated release of Ali and Rux under physiological conditions. In addition, Ali-Rux partly presented degradation after 12 hours of exposure to simulated gastric fluid and simulated intestinal fluid (fig. S12). To visualize cellular internalization, Ali-Rux was conjugated with fluorescein isothiocyanate (FITC) to form trackable FITC-Ali-Rux. After 6 hours of coincubation, intense fluorescent signals from FITC-Ali-Rux were detected in 4T1 cells (Fig. 2H), which was 4.6-fold higher than free FITC (fig. S13), consistent with the HPLC results (fig. S14). Next, we investigated the biodistribution and pharmacokinetics of Ali-Rux with oral administration. After 8 hours, concentration of both Ali and Rux within tumor was notably higher in the Ali-Rux group in comparison with the Ali + Rux group (Fig. 2I and figs. S15 and S16). Furthermore, Ali-Rux showed prolonged blood circulation time than free Ali and Rux (fig. S17). These results collectively confirmed that Ali-Rux improved the tumor enrichment of Ali and Rux through the advantages of nanocrystals.

To investigate the ability of Ali-Rux to induce senescence, SAβG activity was detected in 4T1 cells and MCF-7 cells after 3 days of coincubation with Ali plus Rux and Ali-Rux. Higher SAβG activity was detected in the cells treated with Ali-Rux than in those treated with Ali plus Rux (Fig. 3, A and B, and fig. S18), indicating that Ali-Rux induced more senescence than Ali plus Rux due to improved transport across the cell membrane. Furthermore, Ali-Rux induced less senescence on mouse fibroblast L929 cells than that on 4T1 cells and MCF-7 cells, suggesting the selective induction of senescence on cancer cells by Ali-Rux (fig. S19). Notably, Ali, Ali + Rux, and Ali-Rux led to a subtantial inhibition of the proliferation of 4T1 cells and MCF-7 cells but induced apoptosis in <10% of 4T1 cells (fig. S20), suggesting that senescence might be the major reason for the reduction in cancer cell proliferation. As expected, Ali-Rux exhibited a stronger inhibition on the proliferation of cancer cells than Ali and Ali plus Rux owing to its better induction of senescence. Given the increased antigen presentation of senescent cells (*35*), we analyzed the major histocompatibility complex class I (MHC-I) expression in 4T1 cells and MCF-7 cells after incubation with Ali-Rux by flow cytometry. As illustrated in Fig. 3C and fig. S21, Ali-Rux led to a substantial up-regulation of classical MHC-I molecules, as indicated by flow cytometry of H-2Kb/Db in 4T1 cells and HLA-A/B/C in MCF-7 cells, which was higher than Ali and Ali plus Rux. To explore whether the up-regulation of MHC-I enhances the actual antigen presentation, the H-2Kb–restricted model ovalbumin (OVA)–derived peptide SIINFEKL was detected in senescent 4T1 cells (Fig. 3D). Compared with nonsenescent 4T1 cells, senescent 4T1 cells induced by Ali-Rux presented more SIINFEKL peptide bound to H-2Kb, suggesting that Ali-Rux might increase an antitumoral immune response by efficiently inducing senescence.

Having demonstrated that Ali-Rux enhanced the immunogenicity of 4T1 cells, we sought to investigate whether Ali-Rux could elevate the level of danger signals to recruit and activate immune cells.

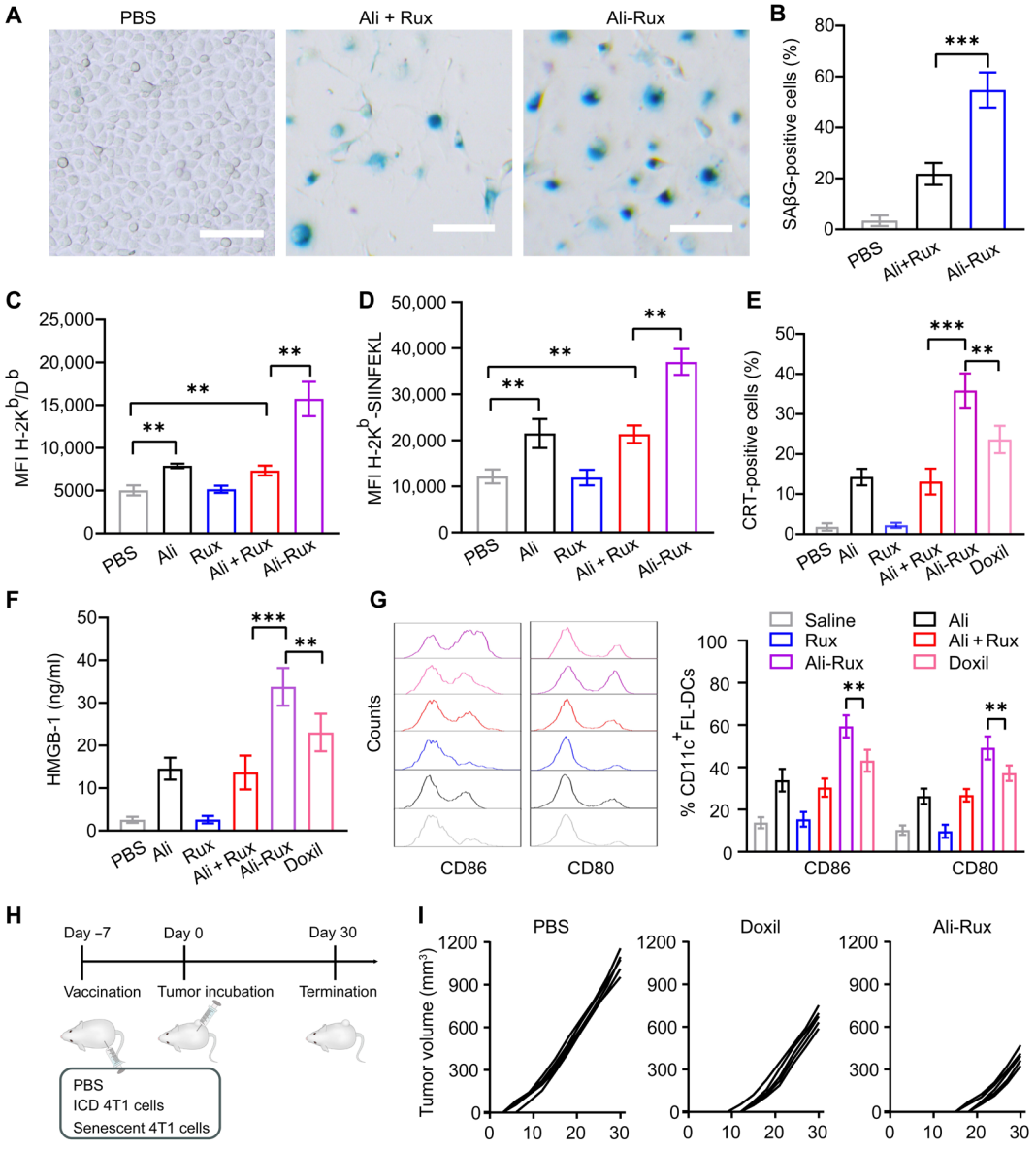

Fig. 3. Senescent 4T1 cells induced by Ali-Rux elicit an antitumor immune response. (**A**) Representative images of SAβG staining in 4T1 cells after treatment with PBS, Ali plus Rux, or Ali-Rux for 3 days. Scale bars, 100 μm. (**B**) Percentage of SAβG-positive 4T1 cells after treatment with PBS, Ali plus Rux, and Ali-Rux for 3 days, $n = 5$, ***$P < 0.001$. (**C**) Flow cytometry analysis of H-2Kb/Db expression in 4T1 cells, $n = 3$. (**D**) OVA-derived SIINFEKL peptide bound to H-2Kb presentation in 4T1 cells stably expressing OVA, $n = 3$. (**E**) Percentage of CRT-positive 4T1 cells after treated with PBS, Ali, Rux, Ali plus Rux, Ali-Rux, and Doxil, $n = 5$. (**F**) The amount of released HMGB1 from 4T1 cells measured by ELISA, $n = 5$. (**G**) Measurement of the expression of costimulatory molecules on DCs after coincubation with various treated 4T1 cells for 24 hours, $n = 5$, **$P < 0.01$. (**H**) Illustration of the timeline and the subcutaneous immunization protocol in this research. (**I**) Tumor growth curves from the mice vaccinated with PBS, Doxil-treated 4T1 cells, and Ali-Rux–treated 4T1 cells. All data are mean ± SD.

Considering that ICD is the current gold standard for efficient antitumor immune responses, we triggered the ICD of cancer cells with a high dose of liposomal doxorubicin (Doxil) and compared the release of DAMPs, such as calreticulin (CRT), chromatin-binding protein high mobility group B1 (HMGB1), and adenosine triphosphate (ATP), from senescent cancer cells and cancer cells undergoing ICD. We found that Doxil induced substantial apoptosis but rare senescence in breast cancer cells (fig. S22). After treatment with Ali-Rux, both 4T1 cells and MCF-7 cells induced more CRT exposure as well as higher release of HMGB1 and ATP than the corresponding cells undergoing ICD (Fig. 3, E and F, and figs. S23 and S24). To explore whether Ali-Rux–induced senescent cancer cells could activate dendritic cells (DCs), we cocultured DCs with Ali-Rux–pretreated 4T1 cells or ICD 4T1 cells and then detected the expression of the costimulatory markers CD86 and CD80 on the surface of DCs. It was found that 4T1 cells pretreated with Ali-Rux induced markedly higher levels of the DC activation and maturation markers CD86 and CD80 than ICD 4T1 cells (Fig. 3G). Previous pioneering studies have demonstrated that senescent cells are more efficient in delivering cellular membrane and cytoplasm material into DCs than ICD cells (*32*, *36*). Consistently, we found that DCs captured more membrane and cytosolic dyes from Ali-Rux–treated 4T1 cells than from ICD 4T1 cells (fig. S25),

suggesting the facile acquisition of tumor-associated antigens from Ali-Rux–induced senescent 4T1 cells by DCs. To further investigate the antitumor immune response of Ali-Rux–induced senescent 4T1 cells, we subcutaneously vaccinated healthy BALB/c mice with Ali-Rux–pretreated 4T1 cells or ICD 4T1 cells and then rechallenged them with 4T1 cells 1 week after immunization (Fig. 3H). The prophylactic effect of Ali-Rux–induced senescent 4T1 cells was markedly better than that of ICD 4T1 cells, which was reflected by the stronger tumor growth delay (Fig. 3I). Furthermore, immunization with Ali-Rux–pretreated 4T1 cells induced greater DC maturation and activation than immunization with ICD 4T1 cells (fig. S26). Collectively, these results indicated that the induction of senescence by Ali-Rux is superior to the induction of ICD by Doxil in releasing DAMPs and triggering DC activation and maturation to improve the antitumor immune response.

We next explored the ability of Ali-Rux to induce tumor senescence and reprogram SASPs in vivo. 4T1 tumor–bearing mice were orally administered Ali, Ali plus Rux, and Ali-Rux every day for a total of seven consecutive administration, respectively. Then, the expression of SAβG and Ki67, as well as the secretion of SASPs, was detected 2 days after the final administration. Consistent with the in vitro findings, Ali-Rux increased SAβG activity while decreasing the proliferative marker Ki67 compared with Ali plus Rux in tumor tissues (Fig. 4, A and B). Compared with Ali, Ali-Rux triggered an obvious increase in the secretion of multiple cytokines and chemokines (IL-6, CCL5, and MCP-1) while decreased the secretion of

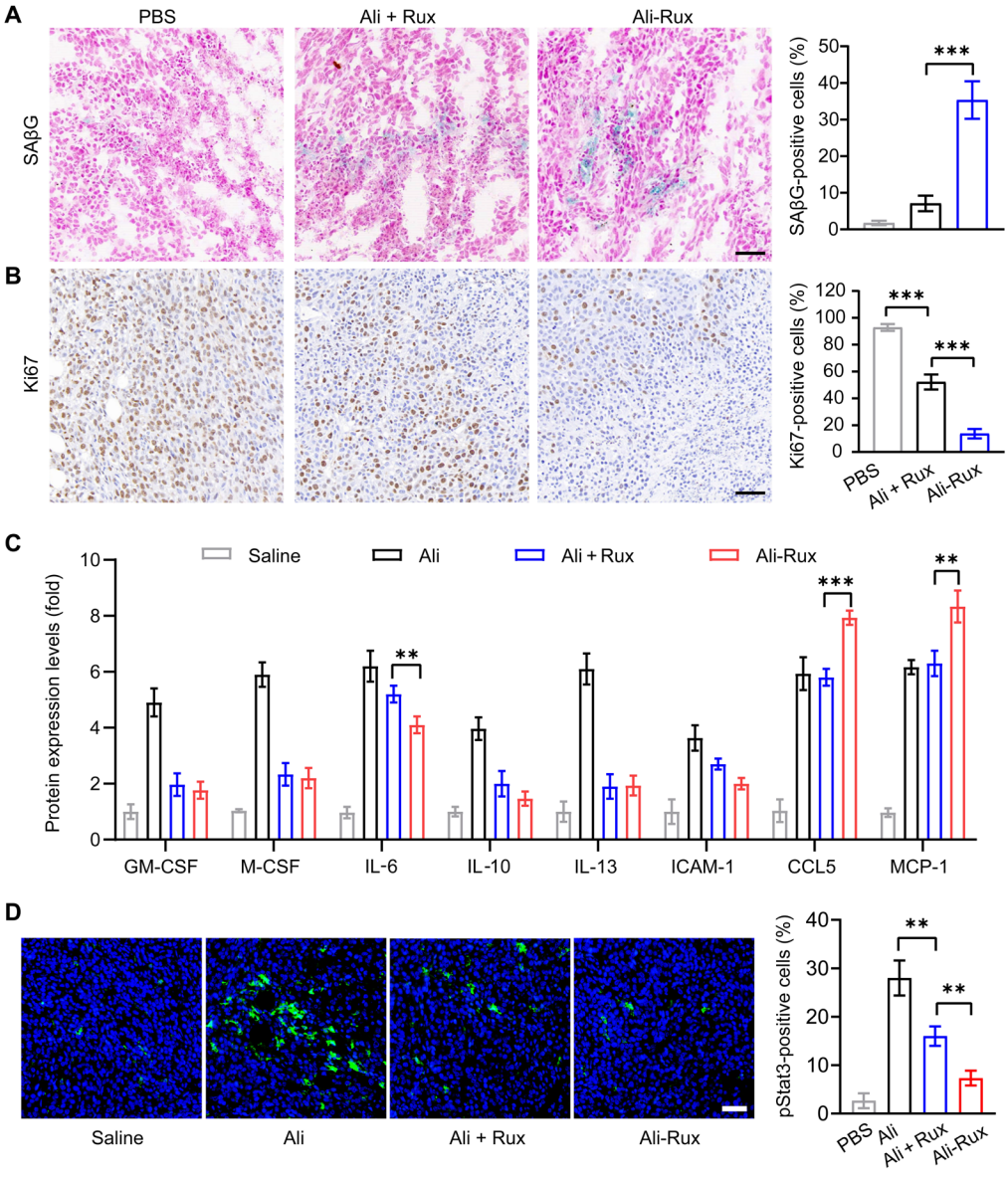

Fig. 4. Ali-Rux induces senescence and reprograms SASPs in vivo. (**A** and **B**) Immunohistochemistry (IHC) analysis of the expression of SAβG (A) and Ki67 (B) in tumors of mice after 7 days of daily oral treatments with saline, Ali (10 mg/kg), Ali (10 mg/kg) plus Rux (15 mg/kg), or Ali-Rux (25 mg/kg). Scale bars, 50 μm, $n = 3$, $^{***}P < 0.001$. (**C**) Quantification of the cytokine protein profile in tumors of mice after 7 days of daily oral treatments with various formulations, $n = 3$, $^{**}P < 0.01$ and $^{***}P < 0.001$. (**D**) IF of the expression of pStat3 (green) in tumors of mice after 7 days of daily oral treatments with various formulations. Scale bar, 50 μm. $^{**}P < 0.01$. All data are mean ± SD.

immunosuppressive factors, including GM-CSF, M-CSF, IL-10, and IL-13, to considerably lower levels (Fig. 4C). To investigate the underlying mechanism, we examined the status of Stat3, an orchestrator of immunosuppressive SASPs in tumors, by IF staining (Fig. 4D). Phosphorylation of Stat3 was up-regulated in 4T1 tumors after treatment with Ali. As a JAK2/STAT3 inhibitor, Rux decreased the activation of Stat3 by Ali in 4T1 tumors. Notably, Ali-Rux induced the lowest level of phosphorylated Stat3 (pStat3). These results together demonstrated that Ali-Rux could trigger a high level of tumor senescence while driving an overall reprogramming of SASPs through the inactivation of Stat3.

In view of the enhanced antitumor immunogenicity and SASP reprogramming, we established 4T1 breast cancer models by injecting 4T1 cells to the mouse mammary fat pads and subsequently investigated the recruitment of immune cells in 4T1 tumors after 7 days of daily oral treatments with various formulations. As shown in Fig. 5 (A and B) and fig. S27, Ali plus Rux and Ali-Rux elevated the influx of $CD8^+$ T cells and NK cells in 4T1 tumors compared with Ali. Ali-Rux triggered the strongest recruitment of $CD8^+$ T and NK cells among all the treatments. $CD8^+$ and NK cells in 4T1 tumors after treated with Ali-Rux were higher cytotoxic than those in the other groups, as characterized by an increase in the expression of CD107a, the level of granzyme B mRNA, and the release of granzyme B proteins (Fig. 5, C to E). Fewer MDSCs were found in 4T1 tumors in the Ali-Rux treatment groups because Ali-Rux inhibited the secretion of immunosuppressive SASPs and thus decreased the recruitment, proliferation, and activation of MDSCs. Knowing that transforming growth factor–β (TGF-β) generated by MDSCs plays a vital role in blocking the proliferation and activation of $CD8^+$ T and NK cells (*37*, *38*), we investigated the secretion of TGF-β in 4T1 tumors after treated with various formulations. The expression of TGF-β was markedly down-regulated by Ali-Rux compared with Ali and Ali plus Rux (Fig. 5F). Furthermore, Ali-Rux resulted in the lowest presence of immunosuppressive M2 macrophages and regulatory T cells (fig. S28). Collectively, these results indicated that Ali-Rux, which integrated prosenescence and SASP reprogramming, effectively enhanced antitumor immunogenicity and reversed the immunosuppressive TME by increasing the number and activity of $CD8^+$ T cells and NK cells and decreasing the frequency of immunosuppressive cells (Fig. 5G).

Considering that Ali-Rux increased the expression of PD-L1 in 4T1 cells and tumors (fig. S29), we investigated the therapeutic effect of Ali-Rux when combined with anti-PD-L1 (αPD-L1) in 4T1 murine breast cancer models (Fig. 6A). The single αPD-L1 failed to inhibit tumor progression or metastasis (Fig. 6, B and C, and fig. S30). Ali modestly delayed tumor growth but ineffectively inhibited tumor metastasis. In contrast, mice receiving Ali plus Rux showed slower tumor growth and fewer pulmonary metastatic nodules than those receiving Ali alone, confirming that the combination of prosenescence and SASP reprogramming could effectively combat tumor metastasis. Consistent with the in vitro data, Ali-Rux showed greater inhibition of primary tumor growth and pulmonary metastasis than Ali plus Rux. In addition, Ali plus Rux notably enhanced the antitumor effect of αPD-L1. Notably, Ali-Rux combined with αPD-L1 exhibited the best therapeutic outcomes, completely eradicating primary 4T1 tumors and suppressing the progression of pulmonary metastatic nodules. To investigate the underlying mechanism, we harvested 4T1 tumors and analyzed the antitumor immune response 3 days after the administration of αPD-L1 (day 18). As shown in Fig. 6 (D to F) and fig. S31, Ali-Rux with αPD-L1 triggered the most pronounced antitumor immune response, including increased infiltration of $CD8^+$ T and $CD4^+$ T cells as well as proinflammatory tumor necrosis factor–α and interferon-γ production. Together, Ali-Rux combined with ICBs resulted in a marked systemic antitumor effect for suppression of the development of both primary and metastatic tumors.

To further explore the effect of Ali-Rux on sensitizing αPD-L1, we screened the dose of Doxil that had the same tumor inhibition rates (52.1%) as Ali-Rux and then compared the therapeutic effect of Ali-Rux and Doxil in combination with αPD-L1. Immunohistochemistry (IHC) and terminal deoxynucleotidyl transferase–mediated deoxyuridine triphosphate nick end labeling staining indicated that Doxil mainly resulted in tumor apoptosis rather than senescence (fig. S32). As expected, Ali-Rux plus αPD-L1 elicited a stronger antitumor effect, more $CD8^+$ T cell infiltration, and higher levels of proinflammatory cytokines (fig. S33), suggesting that Ali-Rux was superior to Doxil in potentiating the therapeutic outcome of ICBs. To investigate whether Ali-Rux with αPD-L1 could establish immune memory to prevent tumor recurrence, recurrent and rechallenge experiments were performed in 4T1 tumor models. 4T1 tumor–bearing mice with almost eradicated primary tumors by Doxil plus αPD-L1 and Ali-Rux plus αPD-L1 were selected on day 30. After another 30 days (day 60), these mice were reinjected subcutaneously with 4T1 cells. The mice whose tumors were removed by surgery were used as controls. The rechallenged tumors grew rapidly in the mice with tumors eradicated by surgery (Fig. 6G). In contrast, mice receiving Ali-Rux plus αPD-L1 or Doxil plus αPD-L1 were protected from local tumor recurrence. Notably, Ali-Rux plus αPD-L1 resulted in lower tumor recurrence and slower tumor progression than Doxil plus αPD-L1. In addition, the generation of effector memory T cells in the mice treated with Ali-Rux plus αPD-L1 was increased by 1.9-fold compared with the control groups on day 60, which was higher than that in the mice treated with Doxil plus αPD-L1 (1.4-fold) (Fig. 6, H and I). Collectively, these results indicated that Ali-Rux plus αPD-L1 could elicit strong antitumor immune memory to prevent tumor relapse.

We lastly evaluated the safety profiles of Ali-Rux plus αPD-L1 in vivo. The body weight of the mice treated with Ali-Rux or Ali-Rux plus αPD-L1 did not decline in comparison to that of the mice treated with saline (fig. S34). The complete blood counts showed that the number of red blood cells, white blood cells, and platelets appeared to be normal upon different treatments (fig. S35). The liver function indices, including alkaline phosphatase, aspartate aminotransferase, and aminotransferase, together with kidney function indices, blood urea nitrogen, and creatinine, in all the treatment groups were within normal physiological ranges. Consistently, hematoxylin and eosin staining and IHC results indicated a lack of pathological injury and senescence in major organs for all the groups (figs. S36 and S37). Collectively, these results suggest the low systemic toxicity of Ali-Rux combined with αPD-L1.

DISCUSSION

SASPs have a double-edged sword effect in regulating tumor immune microenvironment (*39*, *40*). The secretion of proinflammatory SASPs promotes innate and adaptive immune response and triggers tumor-infiltrating CTLs and NK cells to suppress tumor progression. However, uncontrollable accumulation of anti-inflammatory SASPs attracts

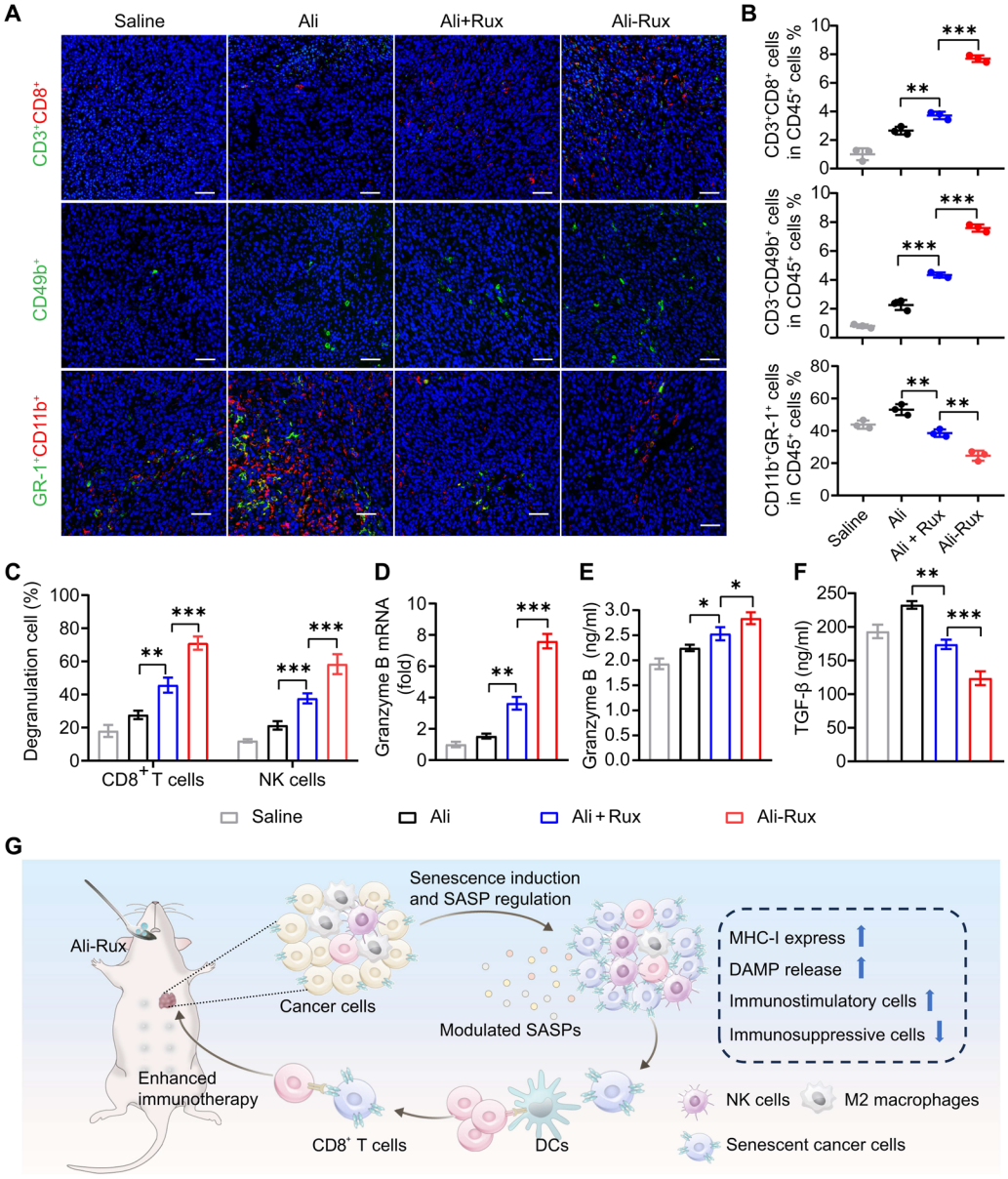

Fig. 5. Ali-Rux remodels the TME. (**A**) 4T1 murine breast cancer models were orally administered saline, Ali (10 mg/kg), Ali (10 mg/kg) plus Rux (15 mg/kg), or Ali-Rux (25 mg/kg) every day for a total of seven consecutive administration. Tumor infiltration of $CD8^+$ T cells, NK cells, and MDSCs was detected 2 days after the final treatments. Scale bars, 50 μm. (**B**) Quantitative flow cytometry of $CD8^+$ T cells, NK cells, and MDSCs in tumors, $n = 3$. $^{**}P < 0.01$ and $^{***}P < 0.001$. (**C**) Quantitative analysis of $CD8^+$ and $NK1.1^+$ degranulation 2 days after the final treatments, $n = 3$. $^{**}P < 0.01$ and $^{***}P < 0.001$. (**D**) The levels of granzyme B mRNA in 4T1 tumors after treated with various formulations 2 days after the final treatments, $n = 3$. $^{**}P < 0.01$ and $^{***}P < 0.001$. (**E**) The secretion of granzyme B, $n = 3$, $^{*}P < 0.05$. (**F**) The release of TGF-β in tumors 2 days after the final treatments, $n = 3$. $^{**}P < 0.01$ and $^{***}P < 0.001$. All data are mean ± SD. (**G**) Schematic illustration that Ali-Rux enhances antitumor immune response through enhancing the expression of MHC-I and release of DAMPs as well as restoring the immunosuppressive TME in orthotopic 4T1 tumor–bearing mouse models.

immunosuppressive cells and generates some growth factors that result in proliferation, invasion, and metastasis of nonsenescent tumor cells. To effectively leverage senescence for cancer treatment, we proposed to regulate senescence homeostasis by maintaining immunostimulatory SASPs and decreasing the context of immunosuppressive SASPs. In such a scenario, the output of SASPs was modulated by the expression of SASP-related gene, including NF-κB, p38MAPK, and JAK2/STAT3 (*41*–*44*). Having screened the effect of NF-κB (BAY), p38MAPK (SB2), and JAK2/STAT3 (Rux) inhibitors on the production of SASPs in Ali-challenged cells, we selected Rux to combine with Ali in a nanocrystal form that facilitated the reduction of protumoral SASPs without interfering with antitumoral SASPs, leading to the robust promotion of tumor immunogenicity. Notably, SASPs are highly heterogeneous across different tumors and different cells within the same tumor (*43*, *45*). Stromal cells treated with same senescent inducers may generate qualitatively and quantitatively different SASPs from cancer cells. Therefore, it is necessary to conduct more comprehensive analysis of SASPs in different tumors and cell

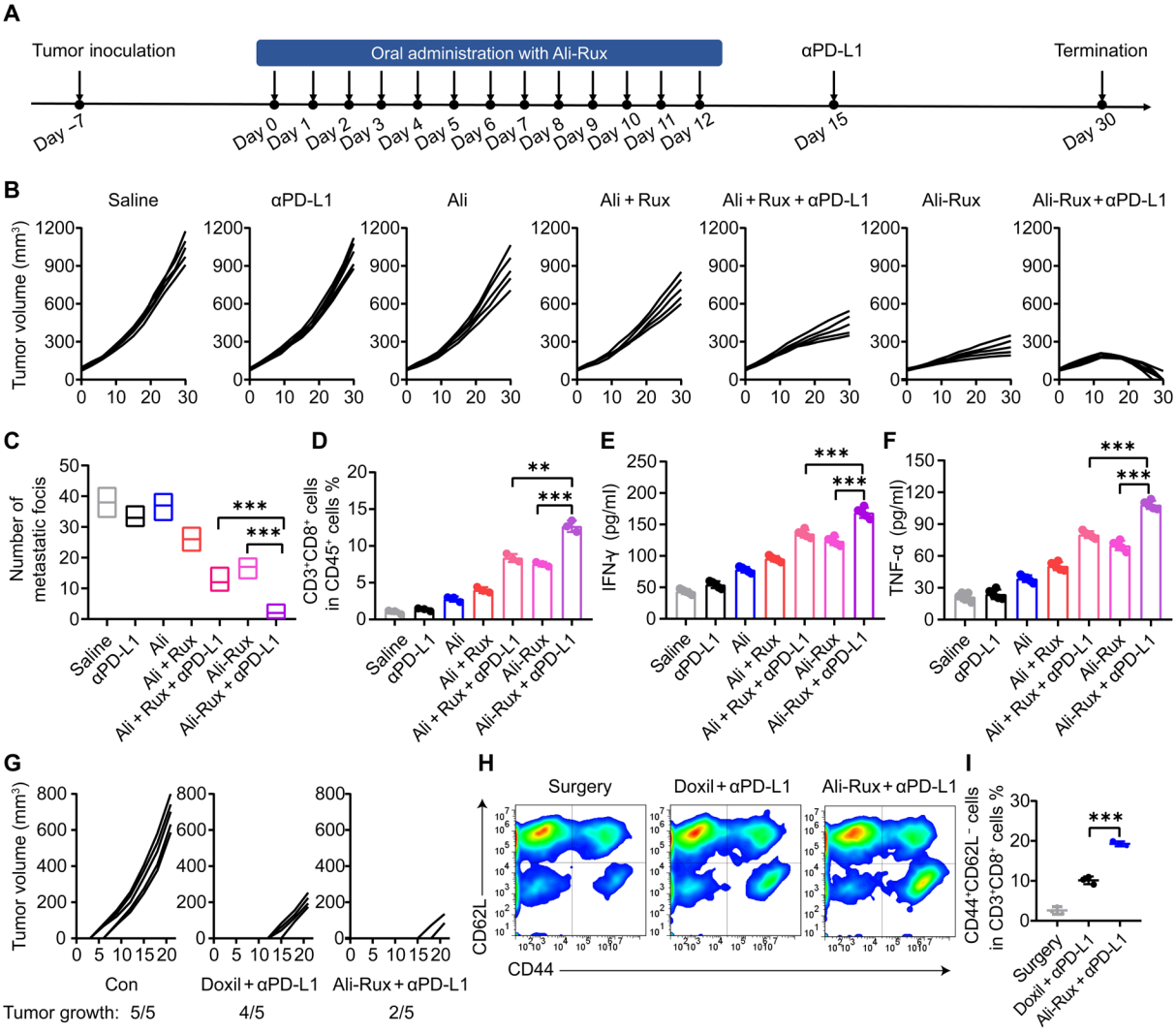

Fig. 6. Therapeutic evaluation of Ali-Rux plus αPD-L1 in vivo. (**A**) Illustration of the timeline for the treatments of 4T1 tumor models. (**B**) Tumor growth curve of the mice after various treatments. (**C**) The number of pulmonary metastatic nodules, $n = 5$, $^{***}P < 0.001$. (**D**) Flow cytometry analysis of tumor-infiltrating $CD8^+$ T cells in various treatment groups, $n = 3$, $^{**}P < 0.01$ and $^{***}P < 0.001$. (**E** and **F**) Secretion of interferon-γ (IFN-γ) (E) and tumor necrosis factor–α (TNF-α) (F) in tumors after treatment with various formulations. $n = 5$. $^{***}P < 0.001$. (**G**) 4T1 tumor–bearing mice whose primary tumors were eradicated by various treatments were rechallenged with 4T1 cells on day 60, and their tumor growth was recorded, $n = 5$. Tumor growth (number of animals developing tumors out of the total) is indicated for each group. (**H** and **I**) 4T1 tumor–bearing mice after treated with Doxil plus αPD-L1 and Ali-Rux plus αPD-L1 for 30 days were selected, and the splenocytes were harvested on day 60 for the analysis of effector memory T cells. Flow cytometry dot plot (H) and quantification (I) of effector memory T cells were shown, $n = 3$, $^{***}P < 0.001$. All data are mean ± SD.

types and considered how senescence ultimately affects tumor progression through stromal remodeling before leveraging senescence for cancer treatment.

In comparison to free drugs, nanocrystals have better bioavailability, improved cellular internalization, and increased tumor accumulation (*46*, *47*). Therefore, we developed a carrier-free nanocrystal consisting of Ali and Rux, which outperformed the mixture of Ali and Rux on tumor senescence induction and SASP reprogramming. The nanocrystals efficiently promoted tumor immunogenicity and reprogrammed immunosuppression in TME by increasing the recruitment and activation of $CD8^+$ T cells and NK cells while decreasing the MDSCs. Benefit from these advantages, the combination of nanocrystals and αPD-L1 elicit a stronger and more durable antitumor immune response to prevent tumor relapse, when compared to the combination of Doxil and αPD-L1. In summary, our study provided a TME reshaping approach by harnessing senescence to potentially complement cancer immunotherapy. We believed that we provide the pioneer about using SASP regulator to manipulate the immunogenic pattern in TME after therapy-induced senescence through coassembled nanocrystals. On these grounds, those simple and low-cost nanocrystals based on senescence inducer and SASP regulator might not only license cancer therapy–induced cellular senescence to improve tumor immunotherapy in an individual manner but also hold great promise for clinical practice by overcoming the challenges of senescence-based cancer immunotherapy.

MATERIALS AND METHODS

Screening SASP regulators

4T1 cells were coincubated with phosphate-buffered saline (PBS), Ali (0.5 μg/ml), Rux (1 μg/ml), Ali (0.5 μg/ml) plus BAY (1 μg/ml), Ali (0.5 μg/ml) plus SB2 (1 μg/ml), and Ali (0.5 μg/ml) plus Rux (1 μg/ml) for 3 days. During the 3-day period, half of the treated cell medium was replaced with fresh cell medium every day. Meanwhile, the replaced cell medium was collected, and the production of SASPs was determined using a cytokine antibody array (Abcam, ab193659) and further quantified by an enzyme-linked immunosorbent assay (ELISA) kit. Afterward, these 4T1 cells were collected, and the cell medium was freeze-dried. Then, female BALB/c mice were injected with 2×10^5 untreated 4T1 cells and the collected medium to the mammary fat pads. The tumors of each mouse were measured by a digital caliper every 3 days, and the tumor volume was calculated by the following formula: tumor volume = tumor length × width^2 × 0.52. After 21 days, all the mice were euthanized, and the tumor tissues were harvested, weighed, and photographed.

Synthesis of Ali-Rux

Ali and Rux were dispersed in independent dimethyl sulfoxide solutions and then premixed in a 2:3 mass ratio (Ali and Rux were 2 and 3 mg/ml in premixed solutions, respectively). The mixed solutions of Ali and Rux flows were introduced into a four-stream multi-inlet vortex mixer through two parallel channels at a flow rate of 5 ml/min each. Deionized water was introduced into the remaining two channels at a flow rate of 50 ml/min each. Ali-Rux was purified through dialysis [Molecular Weight Cut Off (MWCO) = 3.5 kDa].

Biodistribution and pharmacokinetics of Ali-Rux

We injected 5×10^6 4T1 cells into the mammary fat pads of female BALB/c mice to establish 4T1 murine breast cancer models. These 4T1 murine breast cancer models were orally administered Ali plus Rux or Ali-Rux at the same dose of Ali (10 mg/kg). Then, the blood of each mouse was collected at different time points, and the blood circulation of Ali-Rux was analyzed by HPLC. To study the biodistribution of Ali, Rux, and Ali-Rux, mice were euthanized 8 hours after intragastric administration, and tumor tissues and major organs were harvested. Then, the total amount of Ali and Rux was analyzed by HPLC. The 4T1 tumor–bearing mice were orally administered FITC, FITC-labeled Ali, or FITC-labeled Ali-Rux at the same dose of Ali (10 mg/kg). Mice were euthanized 12 hours after oral administration, and blood samples and tumor tissues were collected. Last, the tumor sections were stained with 4′,6-diamidino-2-phenylindole, and fluorescent images were captured via confocal laser scanning microscopy (CLSM).

Induction of senescence by Ali-Rux

4T1 cells and MCF-7 cells were treated with PBS, Ali (0.5 μg/ml) plus Rux (0.75 μg/ml), Ali-Rux (1.25 μg/ml), or Doxil (10 μg/ml) for 3 days. L929 cells were treated with PBS and Ali-Rux (1.25 μg/ml) for 3 days. Then, the SAβG activity was analyzed by using the Cellular Senescence Assay Kit (Millipore) according to the manufacturer's instructions. Cell apoptosis was detected by flow cytometry after costaining with Alexa Fluor 488 annexin V and propidium iodide according to the description of the Alexa Fluor 488 annexin V/Dead Cell Apoptosis Kit (Invitrogen).

4T1 tumor mouse models were orally administered Ali (10 mg/kg), Ali (10 mg/kg) plus Rux (15 mg/kg), and Ali-Rux (25 mg/kg) once daily for 7 days. Then, all the mice were euthanized, and the tumors were harvested. Then, tumors were fixed using 10% formalin and embedded in paraffin according to standard procedures. The tumor sections were stained for Ki67 (clone SP6) and SAβG. For the SASP assay, tumors and major organs were collected and homogenized, and the production of SASPs was determined using a cytokine antibody array (Abcam, ab193659) and further quantified by an ELISA kit in accordance with the manufacturer's protocol. To detect the phosphorylation of STAT3, 4T1 tumors were harvested, formalin-fixed, and paraffin-embedded 4-μm sections. Then, these tumor sections were stained with phospho-Stat3 (Tyr^{705}) (D3A7) for IF assays.

MHC-I antigen presentation

OVA-expressing 4T1 cells and MCF-7 cells were incubated with PBS, Ali (0.5 μg/ml), Rux (0.75 μg/ml), Ali (0.5 μg/ml) plus Rux (0.75 μg/ml), and Ali-Rux (1.25 μg/ml) for 3 days. Then, these cells were washed, trypsinized, and resuspended in 500 μl of PBS. Then, these cells were homogenized using cell lysis buffer (Abcam, ab152163). The cell supernatant was collected and stained with H2Kd/phycoerythrin (PE; 1:400; BioLegend, clone SF1-1.1), HLA-A/B/C, and H2Kb-SIINFEKL (1:200; BioLegend, clone 25-D1.16) at 4°C for 20 min and then measured by flow cytometry.

DAMP release and DC maturation in vitro

To induce senescence, 4T1 cells and MCF-7 cells were incubated with PBS, Ali (0.5 μg/ml), Rux (0.75 μg/ml), Ali (0.5 μg/ml) plus Rux (0.75 μg/ml), or Ali-Rux (1.25 μg/ml) for 3 days. To induce ICD, 4T1 cells and MCF-7 cells were incubated with Doxil (10 μg/ml) for 24 hours. Then, the cell medium was collected, and the secretion of HMGB1 and ATP was detected by an HMGB1 ELISA kit (Elabscience, E-EL-H1554c) and a Chemiluminescence ATP Determination Kit (Beyotime, S0027, China). In addition, the cells were washed with PBS and fixed with 4% paraformaldehyde for 10 min. Subsequently, these cells were stained with FITC-labeled anti-CRT and measured using flow cytometry.

To measure DC maturation, BMDCs were isolated from female BALB/c mice and coincubated with 4T1 cells pretreated with PBS, Ali, Rux, Ali plus Rux, Ali-Rux, or Doxil for 24 hours. Then, BMDCs were collected and stained with anti–CD11c-FITC, anti–CD80-Allophycocyanin (APC), and anti–CD86-PE for 30 min and subsequently analyzed using flow cytometry.

Immunizations with senescent 4T1 cells induced by Ali-Rux

4T1 cells (2×10^5) were treated with Ali-Rux (1.25 μg/ml) for 3 days to induce senescence or Doxil (10 μg/ml) for 24 hours to induce ICD. Then, these senescent 4T1 cells or ICD 4T1 cells were subcutaneously implanted in the flanks of female BALB/c mice. After 1 week, 2×10^5 untreated 4T1 cells were implanted in the opposite flank of these mice. Tumor growth was recorded every 3 days. To detect DC maturation, we harvested popliteal lymph nodes 1 day after immunizations. Subsequently, the lymph nodes were dissociated by pipetting manually, stained with anti–CD11c-FITC, anti–CD80-APC, and anti–CD86-PE for flow cytometry assays.

Therapeutic evaluation

Balb/c female mice (6 to 8 weeks) were purchased from Nanjing Sikerui Biological Technology Co. Ltd. All the animal experiments were conducted in accordance with the guidelines of the Animal Ethics Committee of the Chinese Academy of Sciences (approval number:

SINANO/EC/2023-049). 4T1 murine breast cancer models were randomized into seven groups and then administered saline, αPD-L1 (1.0 mg/kg), Ali (10 mg/kg), Ali (10 mg/kg) plus Rux (15 mg/kg), Ali (10 mg/kg) plus Rux (15 mg/kg) with αPD-L1 (1.0 mg/kg), or Ali-Rux and Ali-Rux (25 mg/kg) with αPD-L1 (1.0 mg/kg). For the αPD-L1 treatment groups, 4T1 murine breast cancer models were intravenously injected with αPD-L1 on day 15. For the Ali, Ali plus Rux or Ali-Rux treatment groups, 4T1 murine breast cancer models were given these drugs once daily by oral gavage. The tumor volume of the mice was detected at predetermined days. All the mice were euthanized on day 30, and the tumors were harvested for weighing.

To compare the effect of Ali-Rux and Doxil in potentiating αPD-L1, 4T1 murine breast cancer models were intravenously injected with various concentrations of Doxil every 3 days from day 0 to day 12. The tumors were harvested on day 15, and the tumor inhibitory rate was determined to screen the dose of Doxil (1.3 mg/kg) that had the same therapeutic effect as Ali-Rux (10 mg/kg). Then, 4T1 murine breast cancer models were intravenously administered Doxil (1.3 mg/kg) every 3 days from day 0 to day 12 and intravenously injected with αPD-L1 on day 15 or orally administered Ali-Rux (10.0 mg/kg) once daily and intravenously injected with αPD-L1 on day 15. Tumor volume was measured every 3 days, and the tumors were harvested on day 18 for analyzing $CD8^+$ T cells and on day 30 for weighing.

Immune memory study

For the immune memory study, the mice whose tumors were removed by surgery, Doxil plus αPD-L1, or Ali-Rux plus αPD-L1 were selected and received subcutaneous injection with 2×10^5 4T1 cells on day 60. The splenocytes were harvested and stained with anti-CD3, anti-CD8, anti-CD44, and anti-CD62L antibodies. Subsequently, the stained cells were analyzed by flow cytometry.

Biosafety evaluation

Normal female BALB/c mice were subjected to oral administration of Ali-Rux (25 mg/kg per mouse) every day for 14 days and intravenous injection of αPD-L1 (1.0 mg/kg per mouse) on day 15. The body weight of the mice was recorded every 3 days. All mice were euthanized after 30 days. Blood was collected from the orbits of the mice in EDTA-coated tubes. Complete blood panel analysis was performed by using an automated hematology analyzer (MEK-6410C, Japan). Serum biochemical parameters were analyzed by a Coulter LX2D (Beckman, Brea, CA). The main organs were sliced and observed by hematoxylin and eosin staining.

Supplementary Materials

This PDF file includes:

Supplementary Text
Figs. S1 to S37
References

REFERENCES AND NOTES

1. K. Esfahani, L. Roudaia, N. Buhlaiga, S. V. Del Rincon, N. Papneja, W. H. Miller Jr., A review of cancer immunotherapy: From the past, to the present, to the future. *Curr. Oncol.* **27**, S87–S97 (2020).
2. D. J. Irvine, E. L. Dane, Enhancing cancer immunotherapy with nanomedicine. *Nat. Rev. Immunol.* **20**, 321–334 (2020).
3. Y. R. Murciano-Goroff, A. B. Warner, J. D. Wolchok, The future of cancer immunotherapy: Microenvironment-targeting combinations. *Cell Res.* **30**, 507–519 (2020).
4. K. Kaur, G. L. Khatik, Cancer immunotherapy: An effective tool in cancer control and treatment. *Curr. Cancer Ther. Rev.* **16**, 62–69 (2020).
5. Y. Zhang, Z. Zhang, The history and advances in cancer immunotherapy: Understanding the characteristics of tumor-infiltrating immune cells and their therapeutic implications. *Cell. Mol. Immunol.* **17**, 807–821 (2020).
6. H. Sadeghi Rad, J. Monkman, M. E. Warkiani, R. Ladwa, K. O'Byrne, N. Rezaei, A. Kulasinghe, Understanding the tumor microenvironment for effective immunotherapy. *Med. Res. Rev.* **41**, 1474–1498 (2021).
7. X. Lei, Y. Lei, J. K. Li, W. X. Du, R. G. Li, J. Yang, J. Li, F. Li, H. B. Tan, Immune cells within the tumor microenvironment: Biological functions and roles in cancer immunotherapy. *Cancer Lett.* **470**, 126–133 (2020).
8. J. E. Bader, K. Voss, J. C. Rathmell, Targeting metabolism to improve the tumor microenvironment for cancer immunotherapy. *Mol. Cell* **78**, 1019–1033 (2020).
9. J. L. da Silva, A. L. S. Dos Santos, N. C. C. Nunes, F. de Moraes Lino da Silva, C. G. M. Ferreira, A. C. de Melo, Cancer immunotherapy: The art of targeting the tumor immune microenvironment. *Cancer Chemother. Pharmacol.* **84**, 227–240 (2019).
10. H. Phuengkham, L. Ren, I. W. Shin, Y. T. Lim, Nanoengineered immune niches for reprogramming the immunosuppressive tumor microenvironment and enhancing cancer immunotherapy. *Adv. Mater.* **31**, 1803322 (2019).
11. M. Datta, L. M. Coussens, H. Nishikawa, F. S. Hodi, R. K. Jain, Reprogramming the tumor microenvironment to improve immunotherapy: Emerging strategies and combination therapies. *Am. Soc. Clin. Oncol. Educ. Book* **39**, 165–174 (2019).
12. J. Wang, Q. Zhang, Y. Li, X. Pan, Y. Shan, J. Zhang, Remodeling the tumor microenvironment by vascular normalization and GSH-depletion for augmenting tumor immunotherapy. *Chin. Chem. Lett.* **35**, 108746 (2024).
13. Z. Wang, F. Chen, Y. Cao, F. Zhang, L. Sun, C. Yang, X. Xie, Z. Wu, M. Sun, F. Ma, D. Shao, K. W. Leong, R. Pei, An engineered nanoplatform with tropism toward irradiated glioblastoma augments its radioimmunotherapy efficacy. *Adv. Mater.* **36**, 2314197 (2024).
14. D. Shao, F. Zhang, F. Chen, X. Zheng, H. Hu, C. Yang, Z. Tu, Z. Wang, Z. Chang, J. Lu, T. Li, Y. Zhang, L. Chen, K. W. Leong, W.-F. Dong, Biomimetic diselenide-bridged mesoporous organosilica nanoparticles as an x-ray-responsive biodegradable carrier for chemo-immunotherapy. *Adv. Mater.* **32**, 2004385 (2020).
15. Z. Zhang, Y.-X. Yue, Q. Li, Y. Wang, X. Wu, X. Li, H.-B. Li, L. Shi, D.-S. Guo, Y. Liu, Design of calixarene-based ICD inducer for efficient cancer immunotherapy. *Adv. Funct. Mater.* **33**, 2213967 (2023).
16. J. Li, W. Cai, J. Yu, S. Zhou, X. Li, Z. He, D. Ouyang, H. Liu, Y. Wang, Autophagy inhibition recovers deficient ICD-based cancer immunotherapy. *Biomaterials* **287**, 121651 (2022).
17. Q. Chen, S. Zhou, Y. Ding, D. Chen, N. S. Dahiru, H. Tang, H. Xu, M. Ji, X. Wang, Z. Li, Q. Chen, Y. Li, J. Tu, C. Sun, A bio-responsive, cargo-catchable gel for postsurgical tumor treatment via ICD-based immunotherapy. *J. Control. Release* **346**, 212–225 (2022).
18. J. Zhu, R. Chang, B. Wei, Y. Fu, X. Chen, H. Liu, W. Zhou, Photothermal nano-vaccine promoting antigen presentation and dendritic cells infiltration for enhanced immunotherapy of melanoma via transdermal microneedles delivery. *Research* **2022**, 9816272 (2022).
19. F. Ruan, H. Fang, F. Chen, X. Xie, M. He, R. Wang, J. Lu, Z. Wu, J. Liu, F. Guo, W. Sun, D. Shao, Leveraging radiation-triggered metal prodrug activation through nanosurface energy transfer for directed radio-chemo-immunotherapy. *Angew. Chem. Int. Ed. Engl.* **63**, e202317943 (2024).
20. D. Muñoz-Espín, M. Rovira, I. Galiana, C. Giménez, B. Lozano-Torres, M. Paez-Ribes, S. Llanos, S. Chaib, M. Muñoz-Martín, A. C. Ucero, G. Garaulet, F. Mulero, S. G. Dann, T. Van Arsdale, D. J. Shields, A. Bernardos, J. R. Murguía, R. Martínez-Máñez, M. Serrano, A versatile drug delivery system targeting senescent cells. *EMBO Mol. Med.* **10**, e9355 (2018).
21. R. Di Micco, V. Krizhanovsky, D. Baker, F. d'Adda di Fagagna, Cellular senescence in ageing: From mechanisms to therapeutic opportunities. *Nat. Rev. Mol. Cell Biol.* **22**, 75–95 (2021).
22. W. Huang, L. J. Hickson, A. Eirin, J. L. Kirkland, L. O. Lerman, Cellular senescence: The good, the bad and the unknown. *Nat. Rev. Nephrol.* **18**, 611–627 (2022).
23. D. V. Faget, Q. Ren, S. A. Stewart, Unmasking senescence: Context-dependent effects of SASP in cancer. *Nat. Rev. Cancer* **19**, 439–453 (2019).
24. L. Cuollo, F. Antonangeli, A. Santoni, A. Soriani, The senescence-associated secretory phenotype (SASP) in the challenging future of cancer therapy and age-related diseases. *Biology* **9**, 485 (2020).
25. C. R. Chambers, S. Ritchie, B. A. Pereira, P. Timpson, Overcoming the senescence-associated secretory phenotype (SASP): A complex mechanism of resistance in the treatment of cancer. *Mol. Oncol.* **15**, 3242–3255 (2021).
26. H. Liu, H. Zhao, Y. Sun, Tumor microenvironment and cellular senescence: Understanding therapeutic resistance and harnessing strategies. *Semin. Cancer Biol.* **86** (Pt 3), 769–781 (2022).
27. M. Takasugi, Y. Yoshida, N. Ohtani, Cellular senescence and the tumour microenvironment. *Mol. Oncol.* **16**, 3333–3351 (2022).
28. M. P. Mongiardi, M. Pellegrini, R. Pallini, A. Levi, M. L. Falchetti, Cancer response to therapy-induced senescence: A matter of dose and timing. *Cancer* **13**, 484 (2021).

29. M. K. Ruhland, E. Alspach, Senescence and immunoregulation in the tumor microenvironment. *Front. Cell Dev. Biol.* **9**, 754069 (2021).
30. M. D'Ambrosio, J. Gil, Reshaping of the tumor microenvironment by cellular senescence: An opportunity for senotherapies. *Dev. Cell* **58**, 1007–1021 (2023).
31. L. G. P. L. Prata, I. G. Ovsyannikova, T. Tchkonia, J. L. Kirkland, Senescent cell clearance by the immune system: Emerging therapeutic opportunities. *Semin. Immunol.* **40**, 101275 (2018).
32. I. Marin, O. Boix, A. Garcia-Garijo, I. Sirois, A. Caballe, E. Zarzuela, I. Ruano, C. S.-O. Attolini, N. Prats, J. A. López-Domínguez, M. Kovatcheva, E. Garralda, J. Muñoz, E. Caron, M. Abad, A. Gros, F. Pietrocola, M. Serrano, Cellular senescence is immunogenic and promotes antitumor immunity. *Cancer Discov.* **13**, 410–431 (2023).
33. A. Salminen, Immunosuppressive network promotes immunosenescence associated with aging and chronic inflammatory conditions. *J. Mol. Med.* **99**, 1553–1569 (2021).
34. A. Toso, A. Revandkar, D. Di Mitri, I. Guccini, M. Proietti, M. Sarti, S. Pinton, J. Zhang, M. Kalathur, G. Civenni, D. Jarrossay, E. Montani, C. Marini, R. Garcia-Escudero, E. Scanziani, F. Grassi, P. P. Pandolfi, C. V. Catapano, A. Alimonti, Enhancing chemotherapy efficacy in Pten-deficient prostate tumors by activating the senescence-associated antitumor immunity. *Cell Rep.* **9**, 75–89 (2014).
35. B. I. Pereira, O. P. Devine, M. Vukmanovic-Stejic, E. S. Chambers, P. Subramanian, N. Patel, A. Virasami, N. J. Sebire, V. Kinsler, A. Valdovinos, C. J. Le Saux, J. F. Passos, A. Antoniou, M. H. A. Rustin, J. Campisi, A. N. Akbar, Senescent cells evade immune clearance via HLA-E-mediated NK and $CD8^+$ T cell inhibition. *Nat. Commun.* **10**, 2387 (2019).
36. C. Yang, Y. Chen, J. Liu, W. Zhang, Y. He, F. Chen, X. Xie, J. Tang, S. Guan, D. Shao, Z. Wang, L. Wang, Leveraging senescent cancer cell membrane to potentiate cancer immunotherapy through biomimetic nanovaccine. *Adv. Sci.* **11**, 2400630 (2024).
37. N. Tumino, A. L. Di Pace, F. Besi, L. Quatrini, P. Vacca, L. Moretta, Interaction between MDSC and NK cells in solid and hematological malignancies: Impact on HSCT. *Front. Immunol.* **12**, 638841 (2021).
38. J. Chen, Y. Ye, P. Liu, W. Yu, F. Wei, H. Li, J. Yu, Suppression of T cells by myeloid-derived suppressor cells in cancer. *Hum. Immunol.* **78**, 113–119 (2017).
39. A. Özdemir, Y. D. Ş. Demir, Z. E. Yeşilyurt, M. Ark, Senescent cells and SASP in cancer microenvironment: New approaches in cancer therapy. *Adv. Protein Chem. Struct. Biol.* **133**, 115–158 (2023).
40. A. M. Battram, M. Bachiller, B. Martín-Antonio, Senescence in the development and response to cancer with immunotherapy: A double-edged sword. *Int. J. Mol. Sci.* **21**, 4346 (2020).
41. J. C. Acosta, A. O'Loghlen, A. Banito, M. V. Guijarro, A. Augert, S. Raguz, M. Fumagalli, M. Da Costa, C. Brown, N. Popov, Y. Takatsu, J. Melamed, F. d'Adda di Fagagna, D. Bernard, E. Hernando, J. Gil, Chemokine signaling via the CXCR2 receptor reinforces senescence. *Cell* **133**, 1006–1018 (2008).
42. T. Kuilman, C. Michaloglou, L. C. W. Vredeveld, S. Douma, R. van Doorn, C. J. Desmet, L. A. Aarden, W. J. Mooi, D. S. Peeper, Oncogene-induced senescence relayed by an interleukin-dependent inflammatory network. *Cell* **133**, 1019–1031 (2008).
43. J. Birch, J. Gil, Senescence and the SASP: Many therapeutic avenues. *Genes Dev.* **34**, 1565–1576 (2020).
44. L. Chibaya, J. Snyder, M. Ruscetti, Senescence and the tumor-immune landscape: Implications for cancer immunotherapy. *Semin. Cancer Biol.* **86**, 827–845 (2022).
45. J. A. Ewald, J. A. Desotelle, G. Wilding, D. F. Jarrard, Therapy-induced senescence in cancer. *J. Natl. Cancer Inst.* **102**, 1536–1546 (2010).
46. H. Lu, Z. Ban, K. Xiao, M. Sun, Y. Liu, F. Chen, T. Shi, L. Chen, D. Shao, M. Zhang, W. Li, Hepatic-accumulated obeticholic acid and atorvastatin self-assembled nanocrystals potentiateameliorative effects in treatment of metabolic-associated fatty liver disease. *Adv. Sci.* **11**, 2308866 (2024).
47. J. Zuo, X. Gao, J. Xiao, Y. Cheng, Carrier-free supramolecular nanomedicines assembled by small-molecule therapeutics for cancer treatment. *Chin. Chem. Lett.* **34**, 107827 (2023).
48. F. Neese, F. Wennmohs, U. Becker, C. Riplinger, The ORCA quantum chemistry program package. *J. Chem. Phys.* **152**, 224108 (2020).
49. S. M. D. Rizvi, S. Shakil, M. Haneef, A simple click by click protocol to perform docking: AutoDock 4.2 made easy for non-bioinformaticians. *EXCLI J.* **12**, 831–857 (2013).
50. O. Trott, A. J. Olson, AutoDock Vina: Improving the speed and accuracy of docking with a new scoring function, efficient optimization, and multithreading. *J. Comput. Chem.* **31**, 455–461 (2010).
51. W. Humphrey, A. Dalke, K. Schulten, VMD: Visual molecular dynamics. *J. Mol. Graph.* **14**, 33–38 (1996).
52. T. Lu, Q. Chen, Interaction region indicator: A simple real space function clearly revealing both chemical bonds and weak interactions. *Chem. Methods* **1**, 231–239 (2021).
53. T. Lu, F. Chen, Multiwfn: A multifunctional wavefunction analyzer. *J. Comput. Chem.* **33**, 580–592 (2012).

Acknowledgments

Funding: This work was supported by National Natural Science Foundation of China (32201087 to Zh.Wa.), the Natural Science Foundation of Jiangsu Province (BK20220295 to Zh.Wa.), Natural Science Foundation of Guangdong Province (2024A1515010581 to C.Y.), Suzhou Basic Research Pilot Project (SJC2021004 to R.P.), the Science and Technology Foundation of Suzhou (ZXT2022007 to Zh.Wa.), and the Fundamental Research Funds for the Central Universities (to D.S.). **Author contributions:** Conceptualization: Zh.Wa., C.Y., R.P., and D.S. Methodology: Zh.Wa., Y.C., Zi.Wu., F.C., and D.S. Investigation: Zh.Wa., Y.C., H.F., Zi.Wu., F.C., and D.S. Formal analysis: Zi.Wu., Y.C., H.F., K.X., X.X., J.L., Y.H., L.W., C.Y., and D.S. Software: Zi.Wu., K.X., and D.S. Resources: Zh.Wa., C.Y., R.P., and D.S. Visualization: Zh.Wa., Y.C., C.Y., and D.S. Validation: Zh.Wa., Y.C., H.F., and D.S. Data curation: Zh.Wa. and D.S. Project administration: C.Y., R.P., and D.S. Writing—original draft: Zh.Wa. and D.S. Writing—review and editing: Zh.Wa., R.P., and D.S. Funding acquisition: Zh.Wa., C.Y., R.P., and D.S. Supervision: R.P. and D.S. **Competing interests:** The authors declare that they have no competing interests. **Data and materials availability:** All data needed to evaluate the conclusions in the paper are present in the paper and/or the Supplementary Materials.

Submitted 8 April 2024
Accepted 25 September 2024
Published 1 November 2024
10.1126/sciadv.adp7022